

# Periodic Wrinkle-Patterned Single-Crystalline Ferroelectric Oxide Membranes with Enhanced Piezoelectricity


Guohua Dong, Suzhi Li, Tao Li, Haijun Wu, Tianxiang Nan, Xiaohua Wang, Haixia Liu, Yuxin Cheng, Yuqing Zhou, Wanbo Qu, Yifan Zhao, Bin Peng, Zhiguang Wang, Zhongqiang Hu, Zhenlin Luo, Wei Ren, Stephen J. Pennycook, Ju Li, Jun Sun, Zuo-Guang Ye, Zhuangde Jiang, Ziyao Zhou,\* Xiangdong Ding,\* Tai Min,\* and Ming Liu\*

Self-assembled membranes with periodic wrinkled patterns are the critical building blocks of various flexible electronics, where the wrinkles are usually designed and fabricated to provide distinct functionalities. These membranes are typically metallic and organic materials with good ductility that are tolerant of complex deformation. However, the preparation of oxide membranes, especially those with intricate wrinkle patterns, is challenging due to their inherently strong covalent or ionic bonding, which usually leads to material crazing and brittle fracture. Here, wrinkle-patterned BaTiO<sub>3</sub> (BTO)/poly(dimethylsiloxane) membranes with finely controlled parallel, zigzag, and mosaic patterns are prepared. The BTO layers show excellent flexibility and can form well-ordered and periodic wrinkles under compressive in-plane stress. Enhanced piezoelectricity is observed at the sites of peaks and valleys of the wrinkles where the largest strain gradient is generated. Atomistic simulations further reveal that the excellent elasticity and the correlated coupling between polarization and strain/strain gradient are strongly associated with ferroelectric domain switching and continuous dipole rotation. The out-of-plane polarization is primarily generated at compressive regions, while the in-plane polarization dominates at the tensile regions. The wrinkled ferroelectric oxides with differently strained regions and correlated polarization distributions would pave a way toward novel flexible electronics.

Wrinkle-patterned surfaces have been specially designed and fabricated for miscellaneous functional applications, such as control of reflections or the wettability of a surface,<sup>[1]</sup> tunable adhesion surface,<sup>[2,3]</sup> smart window,<sup>[4]</sup> and responsive microfluidic devices.<sup>[5]</sup> A wide variety of self-assembled metallic and organic thin films on poly(dimethylsiloxane) (PDMS) substrates have been studied because of their excellent flexibility, elasticity, and sizeable thermal coefficient to allow large strain or stress.<sup>[6,7]</sup> Wrinkles form to minimize the energy of the soft/hard bilayer heterostructure under the compressive forces originating from the strain gradient.<sup>[8–10]</sup> On the contrary, wrinkle-patterned oxides have rarely been realized because of their inherent brittleness and poor flexibility and elasticity. Moreover, the wrinkle-patterned ferroelectric membranes offer an ideal platform to explore strain-correlated fundamental phenomena such as flexoelectricity, strain-induced ferroelectric domain evolutions, and phase transitions,

Dr. G. Dong, H. Liu, Y. Cheng, Dr. Y. Zhao, Dr. B. Peng, Prof. Z. Wang, Prof. Z. Hu, Prof. W. Ren, Prof. Z. Zhou, Prof. M. Liu  
The Electronic Materials Research Laboratory  
Key Laboratory of the Ministry of Education & International Center for Dielectric Research  
School of Electronic Science and Engineering  
State Key Laboratory for Mechanical Behavior of Materials  
the International Joint Laboratory for Micro/Nano Manufacturing and Measurement Technology  
Xi'an Jiaotong University  
Xi'an 710049, China  
E-mail: ziyaozhou@xjtu.edu.cn; mingliu@xjtu.edu.cn  
Prof. S. Li, Prof. H. Wu, W. Qu, Prof. J. Sun, Prof. X. Ding  
State Key Laboratory for Mechanical Behavior of Materials  
Xi'an Jiaotong University  
Xi'an 710049, China  
E-mail: dingxd@mail.xjtu.edu.cn

Prof. T. Li, Y. Zhou, Prof. T. Min  
Center for Spintronics and Quantum System  
State Key Laboratory for Mechanical Behavior of Materials  
School of Materials Science and Engineering  
Xi'an Jiaotong University  
Xi'an 710049, China  
E-mail: tai.min@xjtu.edu.cn  
Prof. H. Wu, Prof. S. J. Pennycook  
Department of Materials Science and Engineering  
National University of Singapore  
Singapore 117574, Singapore  
Prof. T. Nan  
School of Electronic and Information Engineering  
Tsinghua University  
Beijing 100084, China  
Prof. X. Wang  
State Key Laboratory of Electrical Insulation and Power Equipment  
Xi'an Jiaotong University  
No. 28 Xianning West Road, Xi'an, Shaanxi Province 710049, China

 The ORCID identification number(s) for the author(s) of this article can be found under <https://doi.org/10.1002/adma.202004477>.

DOI: 10.1002/adma.202004477

as well as the periodic electric potential induced functions in flexible optical and electrical devices.

Ferroelastic ferroelectrics are a unique class of functional oxides with spontaneous electric polarization, where electric dipoles are directly coupled to the mechanical strain through piezoelectric or flexoelectric effects.<sup>[11–13]</sup> Compared to the non-ferroelectric oxides, domain switching or phase transitions in ferroelastic ferroelectrics may lead to highly improved elasticity and flexibility due to better deformation tolerance and energy conservation.<sup>[14–16]</sup> Recently, we have fabricated freestanding membranes of the BaTiO<sub>3</sub> (BTO) oxide that show remarkable elasticity with a maximum recoverable strain of  $\approx 10\%$ .<sup>[17]</sup> The superelasticity of the membranes originates from ferroelectric *a*- and *c*-domain switching and the correlated continuous dipole rotation.

In this work, we have fabricated periodic wrinkle-patterned single-crystalline ferroelectric oxide membranes, incorporating a functional wrinkled surface for the aforementioned potential applications. We adopted a damage-free water-dissolution process<sup>[18,19]</sup> to fabricate wrinkle-patterned ferroelectric BTO membranes. The finely controlled wrinkle patterns, such as parallel, zigzag, and mosaic shapes, have been obtained by applying different anisotropic stress/strain or tuning the interface adhesion conditions.

To evaluate the properties of wrinkle-patterned BTO membranes, we have adopted various characterization methods, from the atomic scale to the microscopic scale. The atomic-resolution strain and polarization mapping by Z-contrast imaging of scanning transmission electron microscopy (STEM) provide clear evidence of the interplay between strain/stress and polarization: in-plane (IP) polarization dominates in the tensile strain region, while out-of-plane (OOP) polarization appears in the compressive strain region. The microscopic domain structures and the local ferroelectric switching dynamics at differently strained regions of the wrinkled patterned BTO membrane were imaged and measured using piezoelectric force microscopy (PFM). The results clearly show that the piezoresponse is stronger, and the imprint of the hysteresis loops is larger, with increased surface strain, especially under compressive stress. Both TEM and PFM observations were corroborated by atomistic simulations, which reveal that the evolution of *a*- and *c*-domains are

significantly affected by the strain and strain gradient distributions over the membrane. The freestanding BTO membranes presented in this work provide not only a functional wrinkle-patterned surface similar to those of polymers or metals but also a periodic electric potential because of the ferroelectricity, which adds an additional control parameter to the functional surface.

The schematic fabrication process of wrinkled BTO membranes is shown in **Figure 1a**. A high-quality epitaxial BTO/Sr<sub>3</sub>Al<sub>2</sub>O<sub>6</sub> (SAO)/SrTiO<sub>3</sub> (STO) (001) heterostructure was first synthesized by the PLD method, and then a freestanding BTO membrane was lifted-off from the STO substrates by an SAO sacrificial layer. Before etching off the SAO layer, a pre-stretched PDMS film was adhered to the BTO to act as a protecting layer to ensure the integrity of the BTO membrane. Releasing the strain in the PDMS substrate created parallel wrinkling of the BTO membrane. Laser scanning confocal optical images of the wrinkled BTO are shown in **Figure 1b,c**, with parallel and zigzag patterns, respectively, which has a periodic compressive/tensile stress pattern. The XRD pattern for the wrinkled BTO indicates a typical tetragonal phase, as shown in **Figure 1d**. It is compared with the XRD patterns of the as-grown BTO/SAO/STO sample (**Figure S1**, Supporting Information) and the flat BTO/PDMS sample (**Figure S2**, Supporting Information). Around the  $2\theta \approx 45^\circ$ , the pair of (002)/(200) diffraction peaks are characteristic of tetragonality. **Figure 1e** and **Figure S3** (Supporting Information) exhibited the reciprocal space map (RSM) around the BTO (002) and ( $\bar{1}03$ ) reflections. The lattice parameters of the wrinkled BTO are found to be  $a = 4.018 \text{ \AA}$  and  $c = 3.996 \text{ \AA}$  from the principal spots, revealing an IP polarization in the wrinkled BTO. The diffraction spots of BTO are obviously displaced, which is related to the domain switching. In such planar film/substrate systems, the mechanical properties of the rigid films and the elastomer substrate play an essential role in generating wrinkles.<sup>[20–22]</sup> In freestanding BTO membranes, their mechanical behavior is closely related to their thickness, which controls surface pattern formation and evolution, as shown in **Figure S4** in the Supporting Information. With the release of pre-strain, the wrinkle-pattern is induced in the BTO layers by uniaxial mechanical strains. **Figure 1f** presents the wrinkle-patterned BTO layers, exhibiting highly diversified styles, including parallel, zigzag, and mosaic patterns. The parallel pattern is formed when the initial tensile stretch of the PDMS substrate is dominantly along the *x*-direction of the film plane. In contrast, the zigzag pattern appears when the initial tensile stretch of PDMS is along both the *x*- and *y*-directions.

The abovementioned optical observations were carried in a planar view of the sample, which is consistent with the observation under scanning electron microscopy (SEM), as shown in **Figure S5** in the Supporting Information. To obtain the cross-section view, we employed the aberration-corrected scanning transmission electron microscopy (STEM). The samples were prepared using a focus ion beam (FIB) through the site-specific cutting of the parallel wrinkle patterns, as shown in **Figure S6** in the Supporting Information. **Figure 2a** gives a low-magnification STEM-HAADF (high-angle annular dark-field) image of one whole concave–convex wrinkle. The width of one wrinkle is  $\approx 4 \mu\text{m}$ . In comparison, the height difference from the concave to the convex regions is  $\approx 1 \mu\text{m}$ , which is consistent with the value measured from the plan-view optical microscopy and PFM (discussed later). **Figure 2b1,2** are enlarged STEM-HAADF

Prof. Z. Luo  
National Synchrotron Radiation Laboratory & CAS Key Laboratory  
of Materials for Energy Conversion  
Department of Physics  
University of Science and Technology of China  
Hefei 230026, China

Prof. J. Li  
Department of Nuclear Science and Engineering and Department  
of Materials Science and Engineering  
Massachusetts Institute of Technology  
Cambridge, MA 02139, USA

Prof. Z.-G. Ye  
Department of Chemistry & 4D LABS  
Simon Fraser University  
Burnaby, BC V5A 1S6, Canada

Prof. Z. Jiang  
The State Key Laboratory for Manufacturing Systems Engineering  
the International Joint Laboratory for Micro/Nano Manufacturing  
and Measurement Technology  
Xi'an Jiaotong University  
Xi'an 710049, China

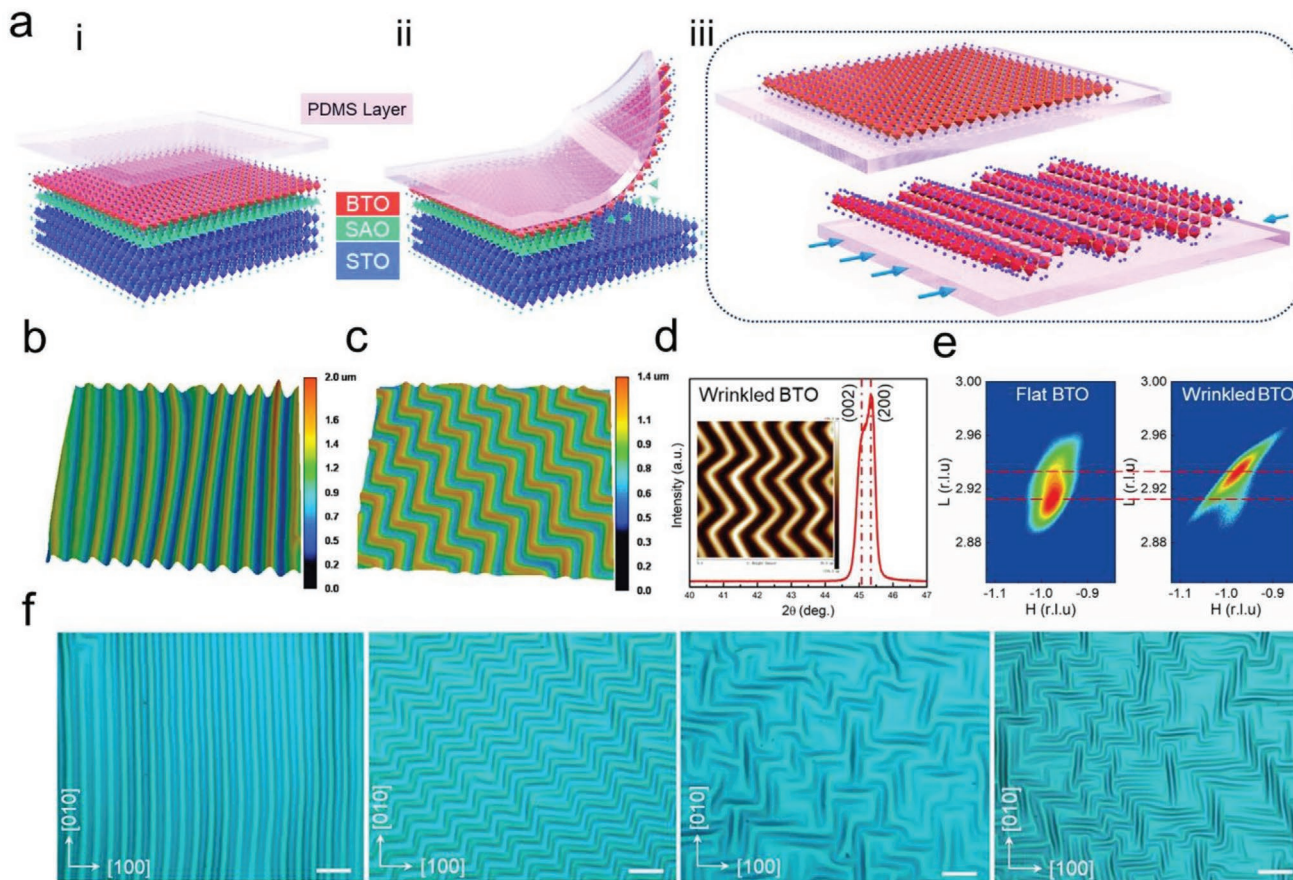


**Figure 1.** Fabrication process of wrinkled BTO membrane. a) Schematic and b,c) laser scanning confocal optical images of wrinkled BTO with parallel and zigzag patterns, respectively. d) XRD patterns of wrinkled BTO membranes on PDMS substrates. e) Reciprocal space map (RSM) of flat and wrinkled BTO around the  $(\bar{1}03)$  reflections. f) Optical microscopy images of wrinkled BTO, giving rise to various patterns (parallel, zigzag, and mosaic). Scale bars are 20  $\mu\text{m}$ .

images of a concave and a convex section, respectively. The thickness of the wrinkled BTO film is  $\approx 50$  nm.

To directly probe the lattice strain and atom displacements within the unit cells of such a concave–convex wrinkle, atomically resolved images are acquired with STEM. HAADF images focusing on the concave and convex regions, as marked in Figure 2b1,2, are shown in Figure 2c1,2, respectively. It is clearly shown that the concave region possesses a compressive strain zone on the top and a tensile strain zone on the bottom, while a convex region with reverse strain zones, as outlined by the red and dashed lines in both images. The STEM imaging mode, compared with the normal TEM mode, produces contrast interpretable by Z contrast (the signal is roughly proportional to  $Z^2$  for HAADF),<sup>[23]</sup> which allows, quantitative analysis of lattice strain and atom displacements within the unit cells, as demonstrated in such perovskites as,  $\text{PbTiO}_3$ ,<sup>[24]</sup>  $\text{BaTiO}_3$ ,<sup>[25,26]</sup> and  $(\text{K,Na})\text{NbO}_3$ .<sup>[27]</sup> Figure 2e1,2 present the lattice parameter analysis, i.e., strain analysis, along IP and OOP directions of Figure 2d. The results show that the compressive strain zone possesses a larger lattice dimension along the out-of-plane direction, 0.422 nm versus 0.38 nm, while a smaller lattice dimension along the IP direction, 0.391 nm versus 0.432 nm, compared with the tensile strain zone.

In addition to the strain variation from the compressive to tensile zones, it is also interesting to determine the atom

displacements inside the unit cells, i.e., the mapping of strain and displacement/polarization. Figure 2f shows a map of the center Ti atom displacement with respect to the corner Ba atoms,  $\delta_{\text{Ti-Ba}}$ , overlaid on a STEM HAADF image from the marked purple rectangular region in Figure 2c1. It shows that the compressive strain zone contains polarization along the OOP direction. In contrast, the tensile strain zone contains polarization along the IP direction. In these two states, the polarization rotates gradually and continuously in 3D within the plane and also out of the plane (the arrows with small lengths). For ferroelectric  $\text{BaTiO}_3$ , the relative displacement of the center Ti atom with respect to the center of its corner Ba atoms reflects the local polarization, as explained in Figure S7 in the Supporting Information. The local  $P_S$  can be roughly estimated using a linear relation for  $\delta_{\text{Ti-Ba}}$ ,  $P_S = k\delta_{\text{Ti-Ba}}$ , where  $k$  is a material-dependent constant deduced from bulk measurements.<sup>[28]</sup> For  $\text{BaTiO}_3$ ,<sup>[25]</sup>  $k$  is around  $1900 \mu\text{Ccm}^{-2} \text{nm}^{-1}$ . The maximum  $\delta_{\text{Ti-Ba}}$ , obtained close to the edge of compressive/tensile strain zones, is  $\approx 29$  pm, much larger than that of  $\approx 13$  pm in bulk. Then the maximum polarization is estimated to be  $\approx 55 \mu\text{Ccm}^{-2}$ . Combining the maximum strain and polarization differences between the compressive and tensile strain regions, the flexoelectric coefficient can be further estimated (see Note S1 and Figures S8–S11 in the Supporting Information).

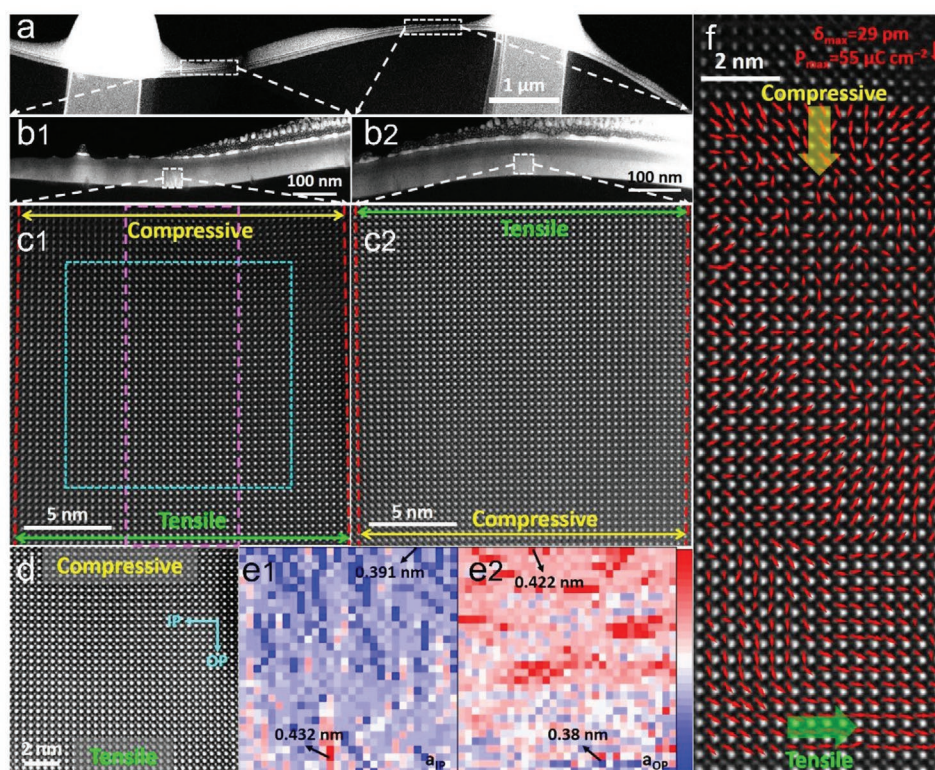


**Figure 2.** STEM images and analysis of polarization and strain. a) Low-magnification STEM HAADF image of one whole concave–convex wrinkle. b1,2) STEM HAADF images of a concave and a convex section, respectively. c1,2) Atomically resolved STEM HAADF images of a concave region with a compressive strain zone on the top and a tensile strain zone on the bottom, and a convex region with reverse strain zones, respectively. d) Atomically resolved STEM HAADF image from the blue square region in (c1). e1,2) Lattice parameter analysis along the IP and OOP directions, showing that the compressive strain zone possesses a larger lattice dimension along the out-of-plane direction and a smaller lattice dimension along the in-plane direction, compared with the tensile strain zone. f) Atomic displacement and polarization arrow map overlaid on a STEM HAADF image from the purple rectangle region in (c1), showing that the compressive strain zone contains polarization predominantly along the out-of-plane direction, while the tensile strain zone contains polarization predominantly along the in-plane direction.

PFM imaging and spectroscopic measurements were conducted to acquire the pristine polarization state and the local polarization and domain switching dynamics of the wrinkled BTO film, respectively (Figure 3). The wrinkled BTO films show periodically alternating peak and valley morphology. At the same time, the IP and OOP PFM measurements also demonstrate the corresponding periodic variation of the amplitude and phase (Figure 3a,b). On a smaller scale, the PFM images of the peak and valley regions reveal multiple nanodomains (Figure S12, Supporting Information). The valley region (compressive strain/strain gradient) shows the strongest mean piezoresponse in the OOP direction, and the peak region (tensile strain/strain gradient) shows the strongest mean piezoresponse in the IP direction. The polarization of the domains in the valley regions mainly points along the OOP direction, while those in the peak regions primarily points along the IP direction. The different polarization states of the peaks and valleys are also revealed in the surface-potential distribution (Figure S13, Supporting Information). The curvature of the peaks and valleys is an indicator of the magnitude of strain/strain gradient. A sharp peak should exhibit a larger strain than that of a broader peak. The corresponding profiles of the height and PFM amplitude in Figure 3c clearly shows that the piezoresponse is enhanced under a more significant tensile or compressive curvature. The

positive and negative strain/strain gradients associated with the peak and valley curvatures should be the key factor that causes a significant difference in the piezoresponses between the peaks and the valleys. The lattice displacement induced by strain/strain gradient determines the pristine polarization state of the wrinkled BTO. Besides the strain-induced polarization, ferroelectric polarization of the wrinkled BTO/Pt film also could be modulated by defect dipoles (oxygen vacancies) and space charges at the interface<sup>[29,30]</sup> resulting in the different preferential polarization orientations under tensile and compressive strains. The coupling between the strain and the electric polarization should be increased with mechanical curvature. This explains the strongest piezoresponse detected in the region of the maximum strain gradient, where the flexoelectricity must be present. Here, both the piezoelectric and flexoelectric effects contribute to the overall piezoresponse.

Ferroelectric hysteresis is critical evidence of ferroelectric polarization switching. The near 180° change of the phase loop between compressive (C1), tensile (T1), and minimum (F1) strained regions (Figure 3d) indicates the electric field induced polarization switching. The hysteresis loop obtained at the C1 region shows a significant imprint, while F1 and T1 regions show rather symmetric loops. To define the relationship between the curvature and the polarization switching

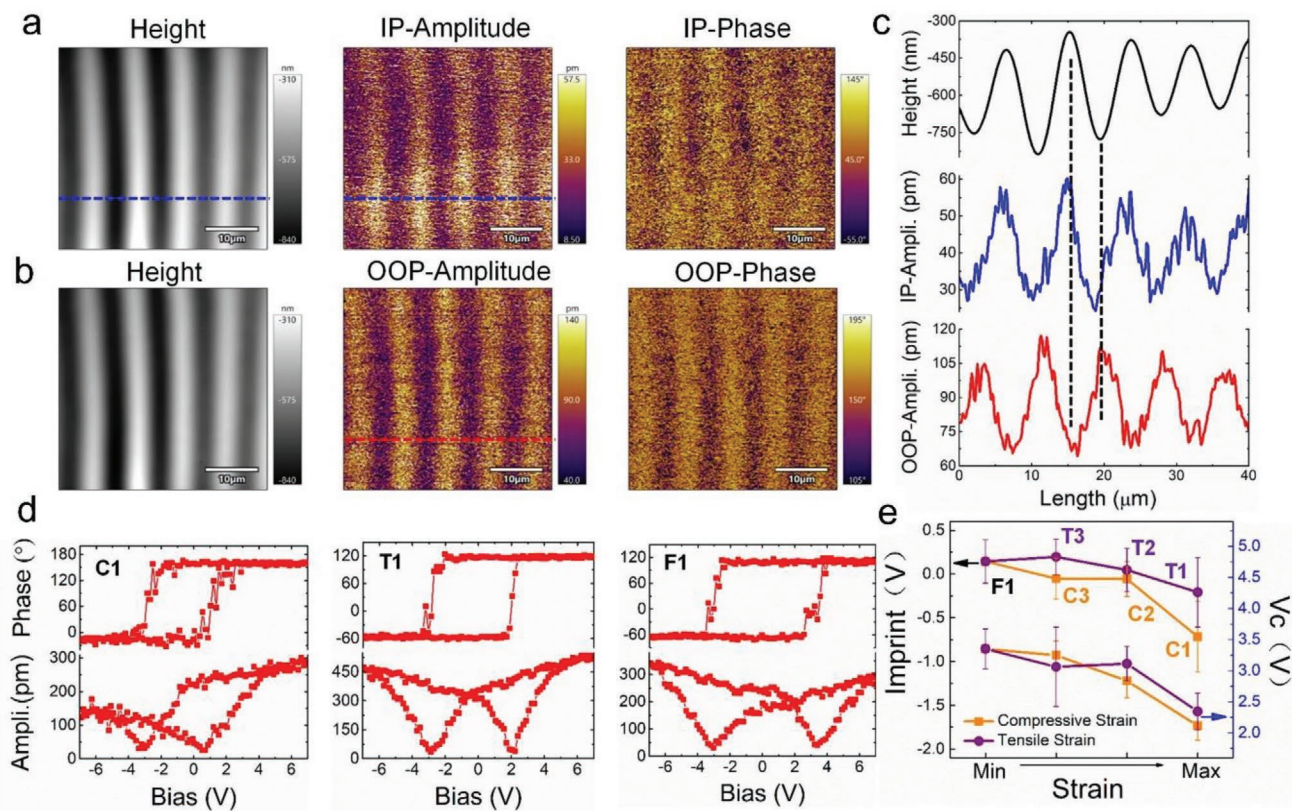


**Figure 3.** PFM images and measurements of wrinkled BTO films. a) IP-PFM images. b) OOP-PFM images. c) Line profiles of the corresponding height and amplitude data (average of 20 pixels) along the blue dotted lines in (a) and (b). d) Representative hysteresis loops of BTO under compressive strain (C1), tensile strain (T1), and a flat region (F1). e) Statistical analysis of the ferroelectric hysteresis loops. Corresponding PFM images and more hysteresis loops are presented in Figure S14 in the Supporting Information. Imprint and coercive bias vary with the strength of the compressive and tensile strain. The error bar is obtained from twelve loops at different locations in each strained region. The smaller the numerical number, the larger the strain level. T: tensile; C: compressive.

characteristics, statistical analyses of the imprints and coercive biases ( $V_c$ ) of the wrinkled BTO under different strain conditions were performed (Figure 3e). Twelve random locations in seven regions (T1: large tensile strain, T2: medium tensile strain, T3: small tensile strain, C1: large compressive strain, C2: medium compressive strain, C3: small compressive strain, and F1: flat region) were chosen to measure the hysteresis loops. The results show that the coercive bias, defined as  $(V_{c+} - V_{c-})/2$ , is reduced under a larger curvature, which indicates easier polarization switching. However, the magnitude of the imprint, defined as  $(V_{c+} + V_{c-})/2$ , is increased in more strained regions, especially for compressive strain, which is close to with previous research.<sup>[31,32]</sup> As expected, the hysteresis loops in the minimum strained regions (flattened regions, F1) are symmetric with negligible imprint. The strain may cause an internal field and domain-wall pinning from elastic defects.<sup>[33]</sup> Apart from the built-in field, stress or strain is also an important factor that directly affects the domain reorientation between the IP and OOP polarizations<sup>[33]</sup> and the flexoelectric effects.<sup>[34,35]</sup> The flexoelectric effects produce asymmetric lattice distortion with preferential polarization direction and trigger the horizontal shift of the hysteresis loops. Therefore, the imprint effect in the strained regions (C1, T1) is higher than in the flat region (F1). Furthermore, one should note that ferroelectric epitaxial

thin films with compressive strain gradients typically exhibit an oppositely self-poled polarization direction, compared with films with tensile-strain gradients.<sup>[36]</sup> This may cause the compressive strain regions (C1) to have a hard polarization direction and thereby a larger imprint effect than the tensile strain region (T1), as observed in the present case.

We further carried out atomistic simulations to explore the microscopic domain structure and local polarization states of the wrinkled BTO membranes (see Methods). We imposed a sine-wave displacement to create a wrinkled pattern as  $y = A \sin(\omega x)$ , where  $A$  is the amplitude and  $\omega$  is the frequency. We constructed a wrinkled configuration with a maximum strain  $\epsilon_{\max}$  of up to 6.0%. Figure 4a–c shows the dipole configurations at different wrinkled states. The  $c$ -domains are widely observed in the initial flat state, with polarization either upward (red arrows) or downward (blue arrows). When the membrane is wrinkled gradually (Figure 4b,c), some dipoles rotate with orientations either left (black arrows) or right (green arrows), indicating a transformation from  $c$ -domains toward  $a$ -domains. The evolution of domain patterns is associated with local stress states. The wrinkled membrane exhibits an obvious strain gradient from compressive strain to tensile strain, exhibiting more like a bending deformation (Figure 4d). As the maximum stress increases, the  $a$ -domains merge and

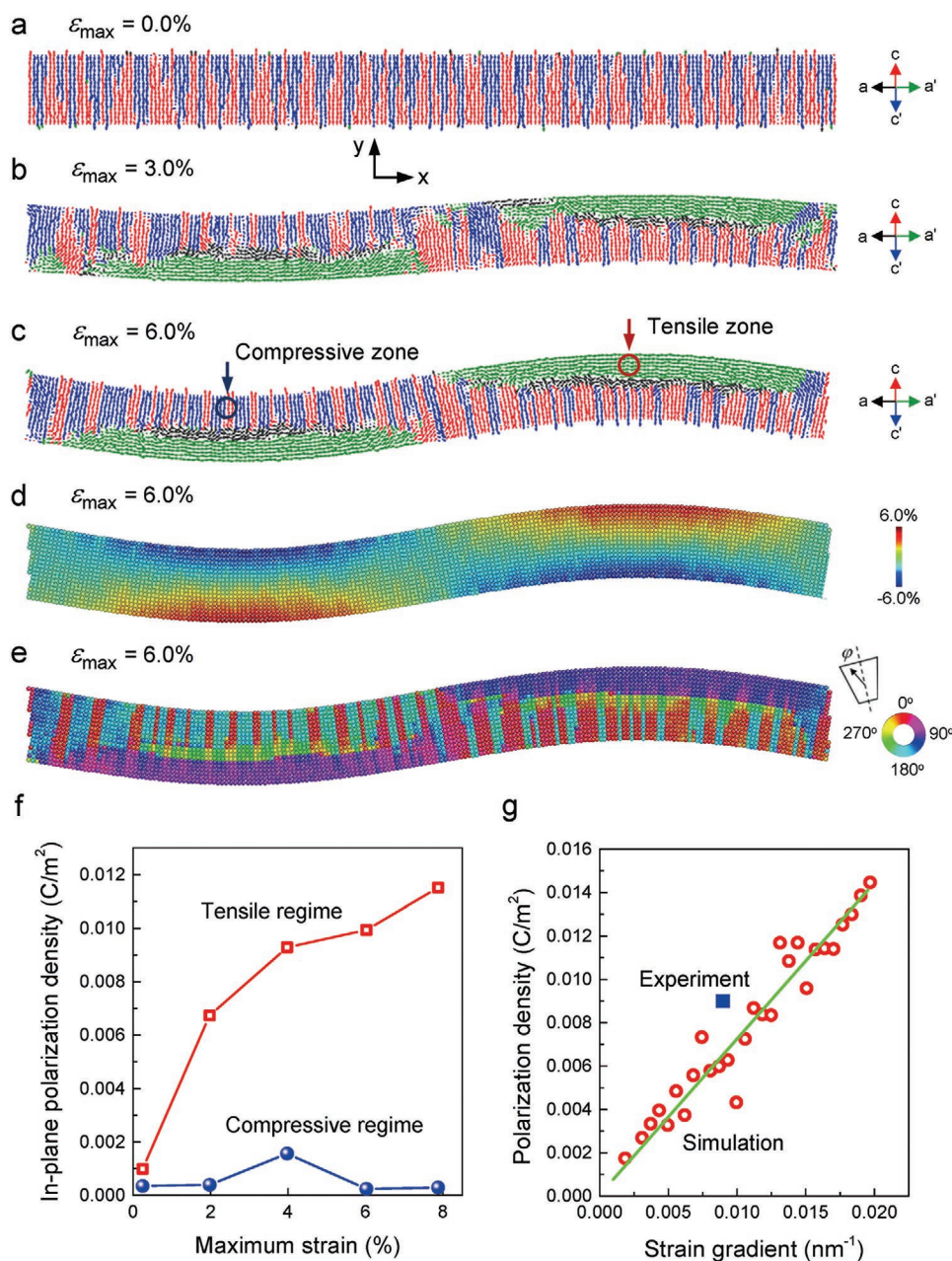


**Figure 4.** Atomistic simulations of the flexibility and flexoelectricity of wrinkled BTO membrane at 300 K. a–c) Typical snapshots of dipole configurations at different strains ( $\epsilon_{\max} = 0\text{--}6.0\%$ ). The green and black arrows represent the dipoles with  $+x$  (left) and  $-x$  (right) components, respectively, in the tensile region. The red and blue arrows represent the dipoles with  $+y$  (up) and  $-y$  (down) components, respectively, in the compressive region. For clarity, the dipole displacements are amplified by a factor of 50. d) The strain map in the wrinkled state ( $\epsilon_{\max} = 6.0\%$ ). e) The distribution of the dipole rotation angle  $\varphi$  away from the central axis of the unit cell ( $\epsilon_{\max} = 6.0\%$ ). f) The variation of local in-plane polarization as a function of maximum strain upon wrinkling. g) The variation of induced out-of-plane polarization as a function of the strain gradient. The blue square is a data point obtained from the experiment.

grow near the free surfaces in the tensile region, while the  $c$ -domains mostly remain in the compressive region with an enhanced polarization density, consistent with the PFM observations (Figure 3). The membrane shows good flexibility even at a larger strain.

Besides the domain switching, more importantly, we found the continuous rotation of dipoles in the transition region connecting  $a$  and  $c$  domains, as demonstrated in our recent

studies.<sup>[17]</sup> We use the rotation angle  $\varphi$ , concerning the central axis of the unit lattice, to characterize the dipole rotation (Figure 4e; Figure S9, Supporting Information). The formation of such a transition zone could effectively eliminate the mismatch stress between  $a$  and  $c$  domains and avoid brittle fracture under a high strain (Figure S10, Supporting Information). We further calculated the IP polarization densities near the free surfaces at the valley (compressive region) and peak

(tensile region) in a local zone with a radius of 2 nm (see the black and red circles and arrows indicated in Figure 4c). Since the *a*- and *c*-domains are preferred at the tensile and compressive regions, respectively, the local IP polarization density increases with the increase of strain at the peak, while it remains at a small value at the valley (Figure 4f). The simulation results are consistent with the PFM measurements above. The dramatic enhancement of the IP polarization density clearly demonstrates the switching of the *c*-domain to *a*-domain in the tensile zone when forming wrinkles.

The present system provides a good platform to investigate the coupling between polarization and strain gradient, known as the flexoelectric effect. A large bending deformation corresponds to a more significant strain gradient with  $\partial\epsilon_{xx}/\partial y = 2\theta/L$ , where  $\theta$  is the bending angle, and  $L$  is the length of the thin film. The induced polarization via the flexoelectric effect is  $P_y = \mu_{xyy}\partial\epsilon_{xx}/\partial y$ , where  $\mu_{xyy}$  is the flexoelectric coefficient. Figure 4g shows the variation of the induced polarization as a function of strain gradient in a local region (Figure S11, Supporting Information). The good linear relationship indicates a typical flexoelectric effect. The blue square shows one data point obtained experimentally (Note S1, Supporting Information), which falls well on the trend of our simulation results. The flexoelectric coefficient in the local area is determined to be  $0.73 \times 10^{-9} \text{ C m}^{-1}$ . Nevertheless, the demonstration of a flexoelectric effect in the wrinkled BTO membranes makes them a valuable form of material for mechano-electric sensing devices.

In conclusion, wrinkle-patterned BaTiO<sub>3</sub>/PDMS membranes have been prepared through PLD growth and the water-dissolution process. The formation of wrinkled BTO membranes results from the excellent superelasticity of the freestanding ferroelectric layer, which originates from ferroelectric domain switching and corresponding continuous dipole rotations. These BTO/PDMS membranes provide an ideal platform to study mechano-electric coupling due to the rich types of strains and inherent strain gradients. In particular, enhanced piezoelectric response and significant flexoelectricity are observed in these wrinkled BTO membranes, which opens the door toward novel flexible ferroelectric devices.

## Experimental Section

**Sample Preparation:** The BaTiO<sub>3</sub>/Sr<sub>3</sub>Al<sub>2</sub>O<sub>6</sub> (BTO/SAO) films were deposited on the SrTiO<sub>3</sub> (001) substrates by a pulsed laser deposition (PLD) system with a KrF excimer laser of 248 nm wavelength. During pulsed laser deposition, the BTO and SAO layers were grown at 750 °C under an oxygen pressure of 13 and 20 Pa. The laser fluence was around 1.8 J cm<sup>-2</sup> and the repetition rate was 3 Hz. The substrate to target distance was 5.0 cm. Before etching off the SAO layer, a pre-stretched PDMS film was adhered to the BTO to act as a protecting layer to ensure the integrity of the BTO membrane. Releasing the strain in the PDMS substrate created the wrinkling of the BTO membrane.

**Piezoresponse Force Microscopy (PFM):** The ferroelectric domain structures were probed by the resonance-enhanced PFM technique (MFP3D, Oxford Instruments, USA). For PFM measurements, 10 nm Pt layer was sputtered on top of the BTO surface before etching of the SAO layer. After freestanding the BTO layer, the Pt layer also formed wrinkles with BTO film coherently. The BTO/Pt heterostructure was transferred to a substrate with a BTO layer on top of the Pt layer. An AC bias was applied to the sample via a conductive probe (PPP-EFM, Nanosensors, Switzerland) near the tip-sample contact resonance frequency, and the

sample surface oscillates accordingly based on the inverse piezoelectric effect. The cantilever detects such oscillation in contact with the sample. The oscillation amplitude and phase signals were recorded, which corresponded to the strength of piezoresponse and the polarization orientation, respectively. The quality and reliability of the imaging were ensured by applying a dual-AC Resonance Tracking (DART)<sup>[37]</sup> technique to track the shift of the contact resonance frequency caused by the surface roughness. For OOP PFM, the OOP deformation of the sample was detected through the OOP deflection of the cantilever. For IP PFM, the IP deformation from shear strain was detected via the torsional motion of the cantilever. The switching spectroscopy PFM measurements reveal the polarization switching dynamics at a fixed location, in which DC pulse swept cycles were applied through the conductive tip to the sample to switch the polarization orientation, while an AC modulation bias was superimposed to detect the amplitude and phase signals simultaneously. The remanent responses were used to display the amplitude loop and phase loop, which indicate the DC field-induced strain loop and the change of polarization orientation, respectively.

**Scanning Transmission Electron Microscopy (STEM):** Aberration-corrected scanning transmission electron microscopy (STEM) studies were conducted using a JEOL ARM200F, equipped with a cold field-emission gun, a new ASCOR 5th order aberration corrector. The STEM samples were prepared by focussed ion beam (FIB), an FEI Versa 3D, through site-specific cutting zigzag and parallel wrinkle patterns. Gatan G2 glue was used to fix the wrinkled BTO film on the Si substrate. This glue was always used to stick two material layers (e.g., oxide thin films) together, and it looks even stronger than many solid materials under ion milling, e.g., Si. Moreover, the voltage and current of each ion milling step was lowered to reduce the ion damage to the sample.

**Molecular Dynamics (MD) Simulations:** The shell model was used to describe the interatomic interactions of BTO systems.<sup>[38]</sup> The basic properties described by this model, such as temperature-induced phase transitions, and spontaneous polarization, keep good agreement with those obtained by experimental measurement and ab initio calculations. A single-crystalline BTO membrane with the orientations of *x*-[100], *y*-[010], and *z*-[001] was constructed. The thickness of the membrane was 8 nm. The aspect ratio was 10. To reduce the high computing cost for the calculations of long-range interactions, a quasi-2D model with only one lattice unit was created in the *z*-direction. Periodic boundary conditions were applied along the *x* and *z* directions, and free boundary conditions were applied in the *y*-direction. The length of the neutral strain line was fixed at 80 nm. The polarization density was calculated as  $P = qs/V$ , where  $q$  is the charge of Ti,  $s$  is the total net displacement in the whole system, and  $V$  is the system volume. Here  $q = 3.072 \times 10^{-19} \text{ C}$  in the current shell model. All the simulations were carried out at 300 K using the Nosé–Hoover thermostat with the LAMMPS code.<sup>[39]</sup> The atomic configurations were displayed by AtomEye.<sup>[40]</sup>

## Supporting Information

Supporting Information is available from the Wiley Online Library or from the author.

## Acknowledgements

G.D., S.L., T.L., and H.W. contributed equally to this work. This work was supported by the National Key R&D Program of China (Grant Nos. 2018YFB0407601, 2019YFA0307900, 2017YFA0206202, and 2016YFA0300702), the Natural Science Foundation of China (Grant Nos. 91964109, 11534015, 51802248, and 51802250), China Postdoctoral Science Foundation (Grant No. 2020M673403), the Fundamental Research Funds for the Central Universities (Grant No. xjh012020005), the National 111 Project of China (Grant No. B14040), the National Sciences and Engineering Research Council of Canada (NSERC Grant No. 203773), and the Key R&D Program of Shaanxi (Program No. 2019TSLGY08) and a Singapore Ministry of Education Tier 2 grant

MOE2017-T2-1-129. H.W. would like to acknowledge financial support from Singapore Ministry of Education Tier 1 grant, R-284-000-212-114, for a Lee Kuan Yew Postdoctoral Fellowship. The authors thank the Instrument Analysis Center of Xi'an Jiaotong University.

## Conflict of Interest

The authors declare no conflict of interest.

## Keywords

ferroelectrics, flexoelectricity, freestanding oxides, piezoelectricity, wrinkles

Received: July 1, 2020

Revised: September 6, 2020

Published online:

- [1] H. H. Hou, J. Yin, X. S. Jiang, *Acc. Chem. Res.* **2019**, *52*, 1025.
- [2] T. J. Ma, T. T. Li, L. W. Zhou, X. D. Ma, J. Yin, X. S. Jiang, *Nat. Commun.* **2020**, *11*, 8.
- [3] M. D. Casper, A. O. Gozen, M. D. Dickey, J. Genzer, J. P. Maria, *Soft Matter* **2013**, *9*, 7797.
- [4] S. G. Lee, D. Y. Lee, H. S. Lim, D. H. Lee, S. Lee, K. Cho, *Adv. Mater.* **2010**, *22*, 5013.
- [5] B. Hughes, S. S. Riaz, L. Romita, S. D. Waldman, D. K. Hwang, *Adv. Mater. Interfaces* **2018**, *5*, 1800663.
- [6] J. Jiang, Y. Bitla, C.-W. Huang, T. H. Do, H.-J. Liu, Y.-H. Hsieh, C.-H. Ma, C.-Y. Jang, Y.-H. Lai, P.-W. Chiu, *Sci. Adv.* **2017**, *3*, 1700121.
- [7] L. M. Loong, W. Lee, X. Qiu, P. Yang, H. Kawai, M. Saeys, J. H. Ahn, H. Yang, *Adv. Mater.* **2016**, *28*, 4983.
- [8] H. Hou, K. Hu, H. Lin, J. Forth, W. Zhang, T. P. Russell, J. Yin, X. Jiang, *Adv. Mater.* **2018**, *30*, 1803463.
- [9] J. Y. Chung, A. J. Nolte, C. M. Stafford, *Adv. Mater.* **2009**, *21*, 1358.
- [10] W. H. Koo, S. M. Jeong, F. Araoka, K. Ishikawa, S. Nishimura, T. Toyooka, H. Takezoe, *Nat. Photonics* **2010**, *4*, 222.
- [11] J. F. Scott, *Science* **2007**, *315*, 954.
- [12] L. T. Yang, X. Kong, F. Li, H. Hao, Z. X. Cheng, H. X. Liu, J. F. Li, S. J. Zhang, *Prog. Mater. Sci.* **2019**, *102*, 72.
- [13] M. Ghidini, F. Maccherozzi, X. Moya, L. C. Phillips, W. J. Yan, J. Soussi, N. Metallier, M. E. Vickers, N. J. Steinke, R. Mansell, C. H. W. Barnes, S. S. Dhesi, N. D. Mathur, *Adv. Mater.* **2015**, *27*, 1460.
- [14] G. Catalan, A. Lubk, A. H. G. Vlooswijk, E. Snoeck, C. Magen, A. Janssens, G. Rispens, G. Rijnders, D. H. A. Blank, B. Noheda, *Nat. Mater.* **2011**, *10*, 963.
- [15] Y. Deng, C. Gammer, J. Ciston, P. Ercius, C. Ophus, K. Bustillo, C. Song, R. Zhang, D. Wu, Y. Du, *Acta Mater.* **2019**, *181*, 501.
- [16] Q. Li, Y. Cao, P. Yu, R. K. Vasudevan, N. Laanait, A. Tselev, F. Xue, L. Q. Chen, P. Maksymovych, S. V. Kalinin, N. Balke, *Nat. Commun.* **2015**, *6*, 9.
- [17] G. H. Dong, S. Z. Li, M. T. Yao, Z. Y. Zhou, Y. Q. Zhang, X. Han, Z. L. Luo, J. X. Yao, B. Peng, Z. Q. Hu, H. B. Huang, T. T. Jia, J. Y. Li, W. Ren, Z. G. Ye, X. D. Ding, J. Sun, C. W. Nan, L. Q. Chen, J. Li, M. Liu, *Science* **2019**, *366*, 475.
- [18] D. X. Ji, S. H. Cai, T. R. Paudel, H. Y. Sun, C. C. Zhang, L. Han, Y. F. Wei, Y. P. Zang, M. Gu, Y. Zhang, W. P. Gao, H. X. Huyen, W. Guo, D. Wu, Z. B. Gu, E. Y. Tsymlal, P. Wang, Y. F. Nie, X. Q. Pan, *Nature* **2019**, *570*, 87.
- [19] S. S. Hong, M. Q. Gu, M. Verma, V. Harbola, B. Y. Wang, D. Lu, A. Vailionis, Y. Hikita, R. Pentcheva, J. M. Rondinelli, H. Y. Hwang, *Science* **2020**, *368*, 71.
- [20] J. Genzer, J. Groenewold, *Soft Matter* **2006**, *2*, 310.
- [21] S. Yang, K. Khare, P. C. Lin, *Adv. Funct. Mater.* **2010**, *20*, 2550.
- [22] J. Rodríguez-Hernández, *Prog. Polym. Sci.* **2015**, *42*, 1.
- [23] S. Pennycook, L. Boatner, *Nature* **1988**, *336*, 565.
- [24] Y. Tang, Y. Zhu, X. Ma, A. Y. Borisevich, A. N. Morozovska, E. A. Eliseev, W. Wang, Y. Wang, Y. Xu, Z. Zhang, *Science* **2015**, *348*, 547.
- [25] C. Zhao, H. Wu, F. Li, Y. Cai, Y. Zhang, D. Song, J. Wu, X. Lyu, J. Yin, D. Xiao, *J. Am. Chem. Soc.* **2018**, *140*, 15252.
- [26] N. Shibata, S. D. Findlay, Y. Kohno, H. Sawada, Y. Kondo, Y. Ikuhara, *Nat. Phys.* **2012**, *8*, 611.
- [27] H. Tao, H. Wu, Y. Liu, Y. Zhang, J. Wu, F. Li, X. Lyu, C. Zhao, D. Xiao, J. Zhu, *J. Am. Chem. Soc.* **2019**, *141*, 13987.
- [28] S. Abrahams, S. Kurtz, P. Jamieson, *Phys. Rev.* **1968**, *172*, 551.
- [29] D. Lee, A. Yoon, S. Jang, J.-G. Yoon, J.-S. Chung, M. Kim, J. Scott, T. Noh, *Phys. Rev. Lett.* **2011**, *107*, 057602.
- [30] D. Damjanovic, *Rep. Prog. Phys.* **1998**, *61*, 1267.
- [31] M. D. Pickett, D. B. Strukov, J. L. Borghetti, J. J. Yang, G. S. Snider, D. R. Stewart, R. S. Williams, *J. Appl. Phys.* **2009**, *106*, 074508.
- [32] Y. Chen, Y. En, Y. Huang, X. Kong, X. Zheng, Y. Lu, *Appl. Phys. Lett.* **2011**, *99*, 203106.
- [33] P. Mokrý, A. Tagantsev, J. Fousek, *Phys. Rev. B* **2007**, *75*, 094110.
- [34] A. Gruverman, B. J. Rodriguez, A. Kingon, R. Nemanich, A. Tagantsev, J. Cross, M. Tsukada, *Appl. Phys. Lett.* **2003**, *83*, 728.
- [35] J. Očenášek, H. Lu, C. Bark, C.-B. Eom, J. Alcalá, G. Catalan, A. Gruverman, *Phys. Rev. B* **2015**, *92*, 035417.
- [36] D. Lee, T. W. Noh, *Philos. Collect. R. Soc. London* **2012**, *370*, 4944.
- [37] B. J. Rodriguez, C. Callahan, S. V. Kalinin, R. Proksch, *Nanotechnology* **2007**, *18*, 475504.
- [38] J. M. Vielma, G. Schneider, *J. Appl. Phys.* **2013**, *114*, 174108.
- [39] S. Nosé, *J. Chem. Phys.* **1984**, *81*, 511.
- [40] J. Li, *Modell. Simul. Mater. Sci. Eng.* **2003**, *11*, 173.